



Nanoscale

**Evolution of Near- and Far-Field Optical Properties of Au Bipyramids upon Epitaxial Deposition of Ag**

Journal:	<i>Nanoscale</i>
Manuscript ID	NR-ART-01-2020-000330.R1
Article Type:	Paper
Date Submitted by the Author:	11-Feb-2020
Complete List of Authors:	Xi, Min; Boston University, Chemistry Reinhard, Bjoern; Boston University, Chemistry

SCHOLARONE™  
Manuscripts

# Evolution of Near- and Far-Field Optical Properties of Au Bipyramids upon Epitaxial Deposition of Ag

Min Xi, Björn M. Reinhard

Department of Chemistry and the Photonics Center, Boston University, Boston, MA 02215, United States

## Abstract

Bimetallic plasmonic nanostructures provide composition and spatial distribution of the individual components in the nanostructure in addition to overall size and morphology as degrees of freedom for tuning near- and far-field optical responses. AgAuAg nanorods (NRs) generated through epitaxial deposition of Ag on the tips of Au bipyramids (BPs) are an important bimetallic model system whose longitudinal dipolar plasmon mode first shows a spectral blue-shift upon initial deposition of Ag on the Au BP tips followed by a red-shift after additional deposition of Ag. Here, we quantify the relative contributions from morphological and compositional effects to the far-field spectral shift of the longitudinal and vertical dipolar plasmon modes during the initial deposition of Ag and compare the near-field in Ag and AgAuAg NRs with lengths between  $L = 130 \text{ nm} - 280 \text{ nm}$  under whitelight illumination through electromagnetic simulations. Subsequently, we experimentally characterize the near-field around AgAuAg NRs with lengths between  $L = 88.1 - 749.0 \text{ nm}$  at a constant excitation wavelength of 1064 nm on a silicon (Si) support through scattering type near-field scanning microscopy (sNSOM). We detect Fabry-Perot resonance-like higher order multipolar plasmon resonances whose order and near-field pattern depends on the length and composition of the NRs as well as the refractive index of the ambient medium. We find that under oblique illumination higher order multipolar modes with an even symmetry dominate on the high refractive index Si substrate due to strong electromagnetic interactions between the NR and the substrate.

## Keywords

Bimetallic nanostructure, plasmons, near-field microscopy, Fabry-Perot resonances

## Introduction

Heterogeneous bimetallic nanoparticles (NPs) offer optical,<sup>1</sup> electrical,<sup>2</sup> and catalytic<sup>3</sup> properties that differ from and in some cases exceed those of the individual components due to synergistic interactions between the constituting elements. In addition to changes of the elemental composition and, thus, the effective dielectric function of the NPs, morphological transformations can affect the physicochemical properties and technological applications of the nanomaterials.<sup>3-7</sup> In the area of plasmonics, hybrid nanostructures from gold and silver have received significant interest for their chemical stability and tunable optical properties.<sup>1,3-5,8-17</sup> Previous studies on Ag-coated Au nanostructures revealed that the encasement of a Au core in a Ag shell can shift the localized surface plasmon resonance (LSPR) both to the blue as well as to the red depending on the amount of deposited Ag.<sup>5,12,13,16</sup> It was then also realized that the selective deposition of Ag on {111} Au surfaces in a reaction described as “Living Nanowire Growth” by Mayer *et al*<sup>14</sup> and Cuncheng *et al*,<sup>18</sup> provides an efficient synthetic strategy for high aspect ratio (AR) one-dimensional Au/Ag bimetallic nanorods (NRs). The LSPR of the Au core / Ag shell NRs (AgAuAg NRs) exhibits a systematic red-shift as the AR of the nanostructures is increased.<sup>14,18</sup> The resonance wavelength of a localized surface plasmon in Ag-Au hybrid systems depends both on the effective dielectric function and the morphology of the structure.<sup>19,20</sup> As demonstrated by Zhu *et al*.<sup>12</sup> the initial deposition of Ag on the tips of Au bipyramids (BPs) is a prime example of a system in which both parameters change and cooperate to determine the measured spectral shift. In this manuscript, we model the effect of a gradual reshaping of the Au BP tip through deposition of Au or Ag to quantify the relative contributions from shape and composition to the spectral shifts of both longitudinal and vertical dipolar modes.

Scalable AgAuAg NRs with defined optical properties are also interesting building blocks for plasmonic nanocircuitries that achieve sub-diffraction limit light field control. Especially the combination with silicon (Si) electronics and photonics promises enabling hybrid devices. Due to its high refractive index, a Si substrate is expected to significantly impact the optical near-field around the plasmonic antenna. We, therefore, investigate here through combination of scattering type near-field scanning microscopy

(sNSOM) and electromagnetic simulations the near-field of AgAuAg NRs with different lengths supported on silicon (Si) at a fixed wavelength of 1064 nm. We observed the evolution of standing wave patterns that are consistent with Fabry-Perot resonances induced by guided plasmons.<sup>21–26</sup> Intriguingly, we found that under the chosen experimental conditions of high refractive index substrate and oblique illumination higher order modes show preferentially a symmetric charge distribution along the long NR axis, i.e. that they are even.

## Results and Discussion

Au BPs were synthesized from gold precursor *via* a two steps growth process in cetyltrimethylammonium bromide (CTAB) solution following previously described procedures.<sup>5,13,14</sup> The obtained Au BPs seeds were then purified,<sup>14,27</sup> and transferred into a cetyltrimethylammonium chloride (CTAC) solution in which Ag was epitaxially grown on the seeds. AgAuAg hetero-nanostructures containing different amounts of Ag were obtained by addition of different amounts of Ag precursor.<sup>14</sup> **Figure 1A – C** show exemplary TEM images of Au BP seeds and two different AgAuAg NRs with different amounts of deposited Ag that illustrate the structural evolution from Au BP to AgAuAg NR. Ag deposition is first directed to the tips of the BPs. After the blunting of the BP tips, deposition of additional Ag results in an elongation of the NRs. High-angle Annular Dark Field Scanning Transmission Electron Microscopy (HAADF-STEM) images (**Figure 1D**), elemental maps (**Figure 1E**) and profiles (**Figure 1F**) obtained through energy dispersive x-ray (EDX) spectroscopy, as well as the high resolution TEM (HRTEM) image (**Figure 1G**) confirm the successful formation of AgAuAg hetero-nanostructures and a heteroepitaxial growth of Ag along the  $\langle 220 \rangle$  direction, laterally bounded by  $\{002\}$  planes and terminated by  $\{111\}$  planes as reported previously.<sup>5,28</sup> The width of the synthesized AgAuAg hetero-nanostructures obtained through this highly anisotropic deposition was determined by the width of the Au BP seeds and remained  $\sim 24$  nm under the chosen experimental conditions, independent of the amount of deposited Ag. **Figure 2A** contains the UV-Vis-NIR absorbance spectra and representative TEM images of Au BPs as well as of AgAuAg NRs

obtained with different input concentrations of  $\text{AgNO}_3$ . Additional TEM images are provided in **Figure S1** and **S2**, and an overview of the morphologies, peak wavelengths and spectral widths for the Au BPs and AgAuAg NRs generated in this study is given in **Table S1**.

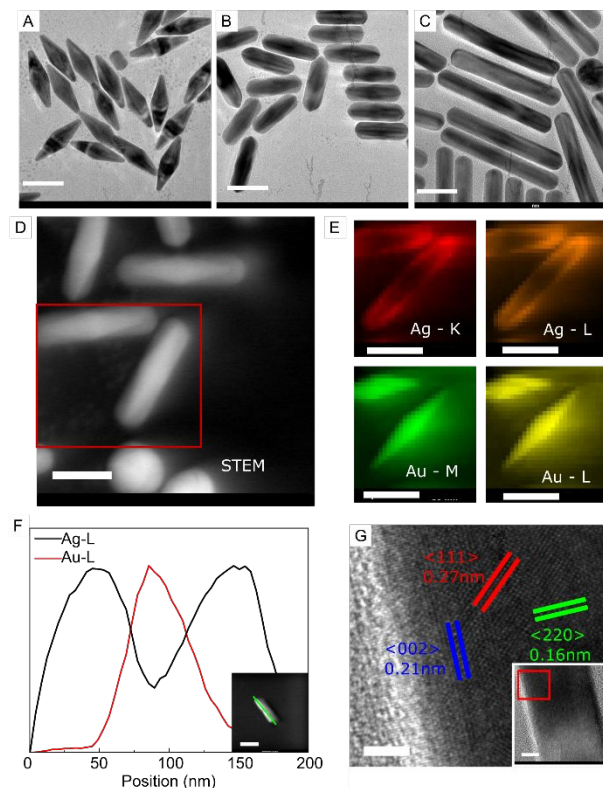


Figure 1. (A) – (C) Representative TEM image of Au BPs (left), and AgAuAg NRs of different amount of Ag deposit (middle and right), scale bars = 50 nm. (D) and (E) HAADF-STEM image and its corresponding elemental mapping of AgAuAg NRs, scale bars = 50 nm. (F) Elemental profile of AgAuAg NR, inset HAADF-STEM image shows the selected AgAuAg NR, and EDS elemental profile was performed along the green line, scale bar = 100 nm. (G) HRTEM image of AgAuAg NR, scale bar = 2 nm (inset HRTEM image shows the structure of AgAuAg NR, scale bar = 5 nm).

The initial deposition of Ag localized around the tips of Au BPs is known to be associated with a strong blue-shift of the dipolar longitudinal plasmon mode.<sup>1,12</sup> In our measurements this shift becomes immediately apparent by comparing the peak resonance wavelength of Au BPs with a length of  $L = 68.5 \pm 1.9$  with that of AgAuAg NRs with  $L = 70.0 \pm 1.6$  nm. The Au BP has a peak resonance of 791 nm, while the peak resonance wavelength of the AgAuAg NRs has shifted to 675 nm (see **Table S1** for a complete list of morphological and far-field characterization results). For the BPs used in this work with  $L = 68.5 \pm 1.9$  nm, width of  $24.3 \pm 0.3$  nm, and tip diameter of  $\sim 5$  nm, the maximum blue-shift of  $\Delta\lambda = -116$  nm

corresponds to a fractional shift of  $\Delta\lambda/\lambda_0 = -116 \text{ nm} / 791 \text{ nm} = -0.147$ . After the deposition of additional Ag, the blue-shift ceases and the resonance starts to red-shift once the restructuring of the BP into a NR with blunted end is complete and deposition of additional Ag increases the length (AR) of the AgAuAg NR. AgAuAg NRs with  $L = 96.0 \pm 3.5 \text{ nm}$  have a peak plasmon resonance wavelength of 697 nm, which is still blue-shifted relative to the Au BPs, but for AgAuAg NRs with  $L = 106.3 \pm 4.1 \text{ nm}$  we measure a peak plasmon resonance of 833 nm, which is longer than that of Au BPs.

**Figure 2B** shows simulated extinction spectra for the evolution of Au BPs to AgAuAg NRs with increasing length, which are in general agreement with the experiment data. Electromagnetic simulations are a useful tool to probe plasmon resonance wavelengths as function of the tip morphology during the initial phase of Ag deposition onto Au BPs. As parameter to quantify the tip morphology, we define the “cone diameter” as the center width of the cone marked with blue lines in **Figure 2C**. The far-field simulation results for the longitudinal dipolar plasmon mode in **Figure 2D** show a continuous spectral blue-shift with increasing cone diameter during the conversion of the sharp BP tip into the rounded NR tip. After the gold tip is completely encased and the BP is converted into a NR, deposition of additional metal at its ends results in an essentially 1-D growth of the NR (**Figure 1C**, **Figure 2E** and **Figure S2A – S2O**). The spectral red-shift of the longitudinal dipolar plasmon resonance associated with an increasing AR once the BP is converted to a NR in both experiment and simulation (**Figure 2F**) follows the expected behavior for plasmonic NR growth.<sup>13</sup>

The experimental spectra show transverse modes in addition to longitudinal modes, albeit with weaker intensity. The transverse dipolar mode blue-shifts from  $\lambda = 528 \text{ nm}$  to 489 nm (summarized in **Table S1**) over the entire range of Ag deposition. The increased peak intensity at  $\sim 400 \text{ nm}$  in the experimental spectra is indicative of transverse multipolar resonances at the lower edge of our spectral range.<sup>12</sup>

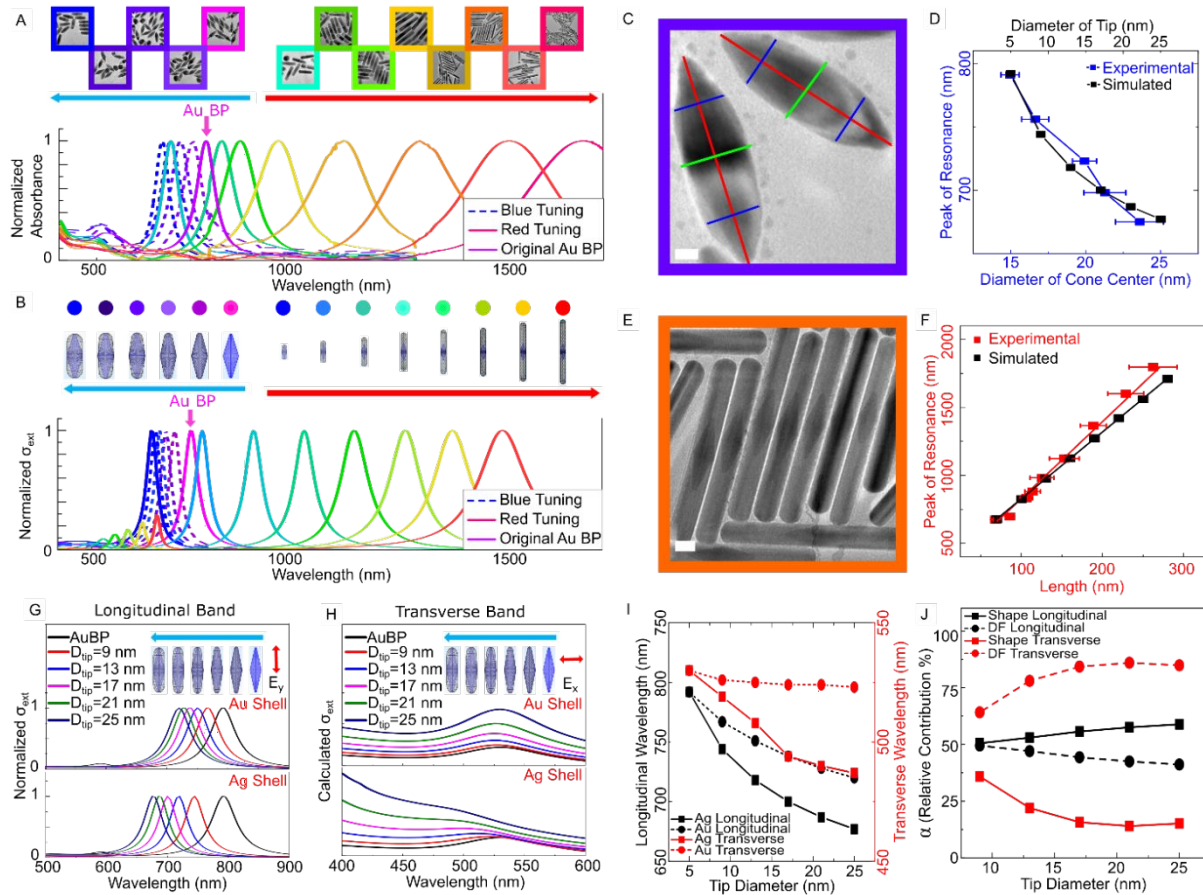


Figure 2. (A) Normalized experimental UV-Vis-NIR spectra for Au BP and AgAuAg NRs with different amounts of deposited Ag. The insets in (A) and additional high resolution TEM images shown in **Figure S1** and **S2** exhibit the morphological changes of the nanoparticles as they evolve structurally. (B) Normalized simulated extinction cross section of Au BP and AgAuAg NRs with different tip radii and lengths. Mesh plots show the evolution of structure associated with a blue and red shift of the spectrum relative to the Au BP reference. (C) Representative TEM analysis shows the length (red line), the width (green line), and the diameter of cone center (blue line) of the imaged AgAuAg bimetallic nanostructures, scale bar = 5 nm. (D) Experimental and calculated resonance peaks of AgAuAg NRs whose peak resonance is blue-shifted relative to that of a Au BP as function cone center diameter. (E) Representative TEM image of a longer AgAuAg bimetallic NR with red-shifted plasmon resonance, scale bar = 20 nm. (F) Experimental and calculated peak resonance wavelengths of AgAuAg NRs whose resonances are red-shifted relative to Au BP as function of length. (G) Simulated spectra (normalized) of the longitudinal dipolar mode of a Au BP core with Au or Ag deposits at the tips with a constant length of  $L = 70$  nm as function of tip diameter. (H) Simulated spectra of the transverse dipolar mode of a Au BP core with Au or Ag deposits with a constant length of  $L = 70$  nm as function of tip diameter. (I) Peak resonance wavelength of longitudinal (black) and transverse (red) dipolar modes of a Au BP core with Au or Ag deposits with a constant length of  $L = 70$  nm as function of tip diameter. (J) Calculated relative contribution ( $\alpha$ ) to the initial blue-shift of the longitudinal (black) and transverse (red) dipolar mode from shape and dielectric function (DF) changes as function of tip diameter in Au BPs on which Ag (change in DF and shape) or Au (change in shape only) is deposited.

A comparison of the simulated spectra of hybrid structures that contain small amounts of either Au (only morphological change) or Ag (morphological change and locally different dielectric functions) selectively deposited on the Au BP tips (**Figure 2G** and **Figure 2H**) quantifies the contributions from changes in the composition and morphology to the initial blue-shift of the longitudinal and transverse dipolar plasmon modes during the early stages of the conversion of the Au BP into a AgAuAg NR. As summarized in **Figure 2I**, the performed simulations predict a maximum blue-shift on the order of 75 nm for the longitudinal dipolar resonance and 10 nm for the transverse dipolar resonance if the tips are restructured through deposition of Au, compared with shifts of 130 nm and 43 nm for longitudinal and transverse dipolar resonances, respectively, for restructuring with Ag. The relative contributions to the blue-shift from the change in morphology, quantified as  $\alpha_{shape} = \frac{\delta\lambda_{Au}}{\delta\lambda_{Ag}}$ , and the change in dielectric function, quantified as  $\alpha_{DF} = 1 - \frac{\delta\lambda_{Au}}{\delta\lambda_{Ag}}$ , is plotted for both longitudinal and transverse dipolar modes as function of tip diameter in **Figure 2J**. The spectral shifts  $\delta\lambda_{Au}$  and  $\delta\lambda_{Ag}$  refer to the blue-shift of the plasmon resonance in Au BP core / Au shell (only morphological change) and Au BP core / Ag shell (change of morphology and dielectric function) structures, respectively. For the longitudinal dipolar resonance, morphological effects (restructuring of the tips) have at least as much contribution to the initial blue-shift as changes in the composition (and dielectric function) due to local deposition of Ag. This is in overall agreement with previous findings from Zhu *et al.*<sup>12</sup>. In contrast, for the transverse dipolar mode the change in the dielectric function clearly dominates. We conclude that for the longitudinal dipolar plasmon mode, the contribution from the morphological change increases with increasing transformation of the tip relative to the shift associated with the change in dielectric function, but for the transverse dipolar mode the change in the dielectric function is the main factor for the blue-shift during the initial stage of Ag deposition.

In longer AgAuAg NRs longitudinal modes of higher order ( $n > 1$ ) can be observed in the extinction spectra. The experimental spectrum of AgAuAg NRs with  $L = 189$  nm in **Figure 3A** shows the dominating fundamental dipolar resonance ( $n = 1$ ) at 1366 nm and two higher order modes ( $n = 2, 3$ ) at 730 nm and 594 nm. The experimental spectrum is in very good agreement with the simulation results for AgAuAg

NRs with similar length ( $L = 190$  nm) in a homogeneous medium with a refractive index of  $n_r = 1.33$  that is also included in **Figure 3A**. It is noteworthy that the even  $n = 2$  mode is excited only under oblique illumination ( $\theta = 45^\circ$ ). The observation of higher order multipolar modes in AgAuAg NRs is consistent with a description of these nanostructures as Fabry-Perot resonators for 1-dimensional guided plasmons.<sup>14,21–26,29,30</sup> Light incident on the NRs induces charge displacements at the nanoscale tips that propagate along the NRs. The propagating plasmons are reflected at the tips before they make it back to their origin. Plasmons that have accumulated a total phase shift of an integer number of  $2\pi$  on their round trip interfere constructively with a new plasmon originating at the same location to form a standing surface plasmon polariton (SPP) wave. This resonance condition is given as:  $2\gamma L(n) + 2\delta\phi = 2\pi n$ ,<sup>29</sup> where  $\gamma$  is the propagation constant,  $L$  is the length of the wire,  $\delta\phi$  is the shift associated with reflection at the ends of the NR,<sup>22</sup> and  $n$  is an integer characterizing the order of the mode. Unlike ideal Fabry-Perot modes described by this formalism, the standing wave modes in the NRs will suffer losses due to Ohmic resistance in the metal, imperfect reflection at the ends of the NRs, and radiative damping.<sup>26</sup>

In **Figure 3B** we summarize the peak energy for the experimental and simulated modes  $n = 1 - 3$  for AgAuAg NRs as well as of the simulated peaks of Ag NRs as function of  $L$  in the range of  $L = 130$  nm – 280 nm. Simulated and experimental data show identical trends; all peaks show a systematic red-shift with increasing length. We note in passing that although both vertical dipolar modes and higher order longitudinal modes lie at higher energies than the longitudinal dipolar mode, the vertical modes blue-shift with increasing  $L$  whereas the higher order modes red-shift. Interestingly, the simulated peak energies for  $n = 1, 2$  are essentially identical for Ag and AgAuAg NRs, but for  $n = 3$ , the AgAuAg NRs lie systematically lower than for the Ag NRs, indicating differences in the mode structure in Ag and AgAuAg NRs. We mapped the near-field ( $|E/E_0|$ ), where  $E_0$  is the incident E-field, for the  $n = 1, 2, 3$  modes of AgAuAg NRs and Ag NRs at selected lengths (**Figure 3C1 – C3**). The simulations were performed for excitation with linearly polarized light whose polarization points along the long axis of the NR. The odd modes with  $n = 1$  and 3 were excited with an angle of incidence of  $90^\circ$ ; while the even  $n = 2$  mode was excited with an angle

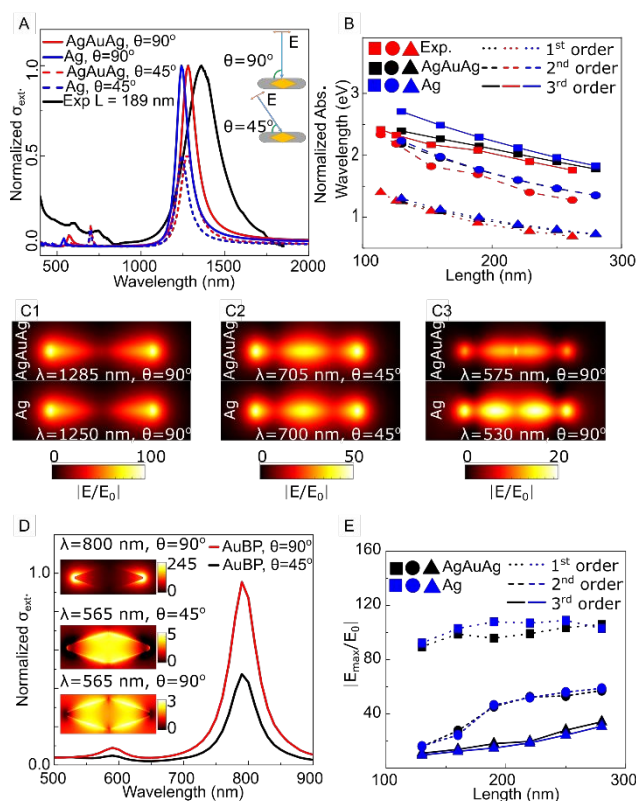


Figure 3. (A) Simulated extinction cross sections of AgAuAg NR and Ag NR with  $L = 190$  nm excited with light incident at an angle of  $90^\circ$  and  $45^\circ$  relative to the long NR axis with the polarization pointing parallel to the long axis of the NR, and experimental measured UV-Vis-NIR spectra for AgAuAg NRs with  $L = 189$  nm. (B) Summary of peak resonance energy for different plasmonic mode orders ( $n = 1, 2, 3$ ) for AgAuAg NRs and Ag NR as function of length,  $L$ . NRs are excited with light incident at an angle of  $90^\circ$  and  $45^\circ$  relative to the long NR axis with the polarization pointing parallel to the long axis of the NR. (C1-3) Normalized E-field map of AgAuAg NR (top) and Ag NR (bottom) with length ( $L = 190$  nm) for  $n = 1, 2, 3$ . The odd modes with  $n = 1$  and  $3$  are excited with an angle of incidence of  $90^\circ$  (see A); while the even  $n = 2$  mode was excited with an angle of incidence of  $45^\circ$ . The depicted plane is the XY center plane of the NR. (D) Simulated extinction cross sections of Au BP with  $L = 70$  nm excited with light incident at an angle of  $90^\circ$  and  $45^\circ$  relative to the long NR axis with the polarization pointing parallel to the long axis of the NR. And the inset E-field maps show the E-field distribution for  $n = 1, 2, 3$ . (E) Comparison of the E-field ( $|E_{\text{max}}/E_0|$ ) enhancement for AgAuAg NRs and Ag NRs for  $n = 1, 2, 3$  as function of length.

of incidence of  $45^\circ$ . The E-field maps of AgAuAg ( $L = 190$  nm) and Ag ( $L = 190$  nm) NRs are shown in **Figure 3C1 – C3**. For  $n = 1$  (**Figure 3C1**) and  $n = 2$  (**Figure 3C2**), the E-field distribution and intensities for AgAuAg and Ag NRs are very similar but for  $n = 3$  (**Figure 3C3**) the AgAuAg NR contain a central region of enhanced E-field, which is absent in the Ag NR. In the presence of the Au BP the E-field gets redistributed and localizes to the edges of the base of the BP. The unique E-field distribution indicates that,

at least in some cases, a patterning of the dielectric function along the NR axis allows for a restructuring of the  $E$ -field. We attribute this effect to the existence of distinct Au BP modes (**Figure 3D**) that in short bimetallic NRs lie in the same wavelength range as the  $n = 3$  mode that can localize the  $E$ -field to the center of the NR.  $E$ -field maps of the  $n = 3$  mode for longer AgAuAg NRs are shown in **Figures S3** and **S4**. The maps in **Figure 3D** reveal that as the length of the AgAuAg NR increases, the  $E$ -field distribution becomes more and more similar to that of the Ag NR with identical length, presumably because the multipolar resonances of the bimetallic NR no longer overlap with modes of the Au BP. **Figure 3E** plots the  $E$ -field enhancement,  $|E_{max}/E_0|$ , for all modes  $n = 1, 2, 3$  in AgAuAg and Ag NRs as function of length  $L$  shows that the peak  $E$ -field enhancements for AgAuAg and Ag NRs are comparable. Although the bimetallic NRs do not provide an increase in peak  $E$ -field intensity, additional degrees of freedom to spatially pattern the  $E$ -field in short AgAuAg NRs could be of potential use in plasmon-based technological applications, such as photothermal therapy, photocatalysis, nanoantenna design, and fluorescence emission control.

To further characterize the near-field of higher order multipolar modes in AgAuAg NRs, we experimentally mapped standing SPP waves in AgAuAg NRs of different lengths deposited on a high refractive index substrate (Si) and excited at a fixed wavelength of 1064 nm by sNSOM. The length of the investigated AgAuAg NRs varied from 88.1 nm to 749.0 nm. Our experimental setup is based on a commercial Neaspec sNSOM is shown in **Figure 4A**.<sup>26–37</sup> The samples were illuminated with s-polarized light at an angle of  $60^\circ$  relative to the normal with a fixed excitation wavelength of 1064 nm, and the near-field scanning was performed with a Pt/Ir coated Si tip in tapping mode. The probe tip was scanned over the sample at a height of approximately 15 nm; p-polarized light scattered by the tip was detected and analyzed through an interferometer. This detection scheme is most sensitive to the z-component of the  $E$ -field in the illuminated nanostructures ( $E_z$ ). The amplitude and phase of the near-field signal scattered by the tip was isolated through lock-in amplification of higher harmonics of the tip oscillation frequency. Unless otherwise noted, we used the fourth harmonic for the analysis of the near-field amplitude and the third harmonic for the phase. **Figure 4B1a – B3a, B1b – B3b** and **B1c – B3c** show topology, scattering

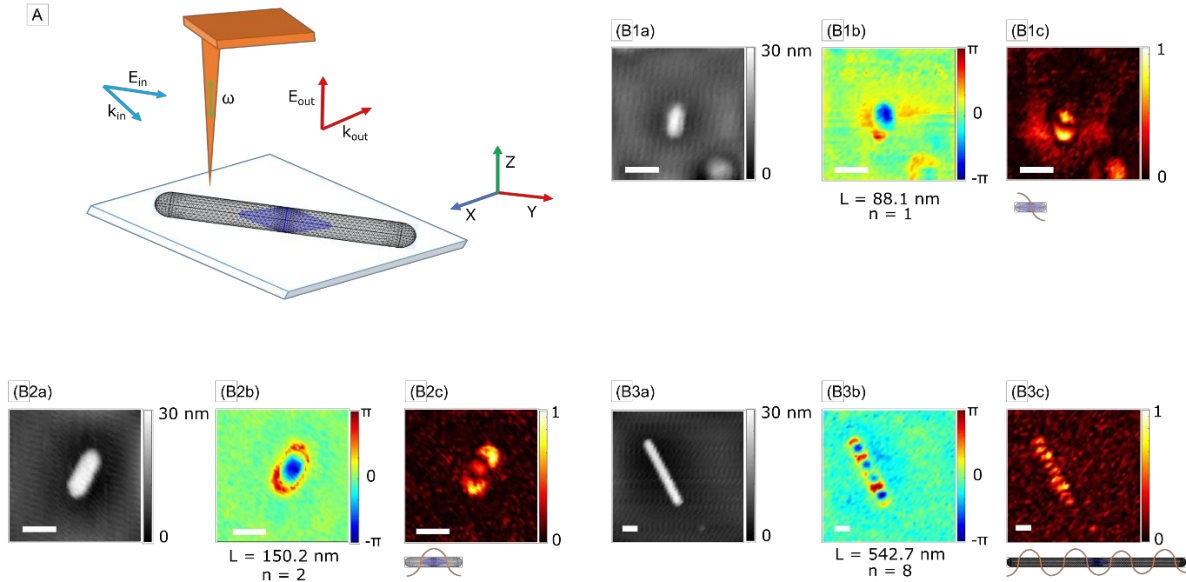


Figure 4. (A) Scheme of the setup; (B1a) – (B3a), (B1b) – (B3b), and (B1c) – (B3c), Representative NSOM measurement results of AgAuAg NR, with measured topography (left), optical phase change (middle), SNSOM signal intensity (right). Scale bars = 50 nm.

phase map, and  $E$ -field amplitude for AgAuAg NRs with lengths of  $L = 88.1$  nm,  $150.2$  nm, and  $542.7$  nm. Additional scans for AgAuAg NRs with lengths of up to  $L = 749.0$  nm are provided in **Figure S5**. Our recorded near-field maps show regions of increased  $E_z$ -field amplitude of opposite phase separated by nodal planes, consistent with the formation of standing waves patterns.<sup>14,29</sup> The  $L = 88.1$  nm structure in **Figure 4B1a – B1c** shows a dipolar distribution with two  $E$ -field maxima (positive and negative) separated by a single nodal plane, corresponding to  $n = 1$ . We detected standing wave patterns up to an order of  $n = 12$  for  $L = 749.0$  nm. **Figures 4B2a – B2c and B3a – B3c** show representative examples of mode orders  $n = 2$  ( $L = 150.2$  nm) and  $n = 8$  ( $L = 542.7$  nm). The sign of the phase at the ends of the NR in **Figures 4B2b and B3b** is identical, which is a characteristic property of an even Fabry-Perot mode.

Intriguingly, all modes with higher orders  $n > 1$  detected in this study were even ( $n = 2, 4, 6, 8, 10, 12$ ). For a plane wave incident normal to the sample plane, the excitation of even orders are symmetry forbidden if the polarization points along the long nanorod axis. This selection rule does, however, not strictly apply to our NSOM measurements due to the oblique angle of incidence<sup>13,26,43–45</sup> (see also **Figure**

**3A)** and the possibility of multiple scattering events at the tip-NR interface.<sup>29,38,46</sup> Although the observation of even modes is therefore not unexpected under the chosen experimental conditions, their predominance for  $n > 1$  is at first surprising. High refractive index substrates facilitate electromagnetic interactions with plasmonic nanoparticles that can perturb plasmon modes or even create entirely new types of plasmon modes. For instance, for Au NRs on a Si substrate a plasmon mode comprised of vertically aligned, in phase oscillating electric dipoles was reported.<sup>47</sup> This particular mode would yield a homogenous charge distribution on the top surface of the NRs, which is not the case for the modes investigated in this work. Our sNSOM measurements of AuAgAu NRs probe the  $E$ -field over the top surface of the NRs and although we find identical sign charge centers at the ends, we still detect a modulation of the surface charge density along the NRs.

In sNSOM the tip scatters the near-field around a nanostructure so that it becomes detectable in the far-field. Neumann *et al.*<sup>38,46,48</sup> applied the reciprocity theorem of electromagnetism to express the detected  $E$ -field as a function of the near-field around the nanostructure excited by the incident light, the tip polarizability, and a virtual local near-field around the nanostructure generated by a point dipole at the detector. Specifically, for the experimental configuration chosen in this work with s-polarized excitation and p-polarized detection, the relevant virtual  $E$ -field component is the p-component which is parallel to the transmission axis of the polarizer in front of the detector. The p-polarized component of the virtual  $E$ -field around the metal NRs can be emulated in electromagnetic simulations by exciting the NRs with p-polarized light with an angle of incidence  $\theta$  that is identical to the scattering angle towards the detector.<sup>38</sup> We simulated the virtual  $E$ -field around AgAuAg NRs and its dependence on the refractive index using p-polarized light with a fixed wavelength of 1064 nm incident from the superstratum (air) (**Figure 5A**). **Figure 5B** maps the  $E$ -field enhancement around a AgAuAg NR ( $L = 290$  nm) on substrates with different refractive indices for  $\theta = 60^\circ$ . The maps confirm enhanced  $E$ -field at both the top and bottom surface, but the  $E$ -field enhancement is substantially stronger at the bottom surface. The enhancement increases with increasing refractive index of the substrate, confirming strong interactions between the metal NR and the

substrate. Surface charge density oscillations in the metal polarize the high refractive index substrate and create charge densities of opposite sign in the high refractive index substrate. This charge distribution enhances the local  $E$ -field at the metal-dielectric interface but attenuates any net dipole moment along the long NR axis and, thus, decreases the optical cross-sections of odd modes.<sup>49</sup> **Figure 5C** shows the extinction cross sections of AgAuAg NRs ( $L = 290$  nm) in the range of 950 – 1175 nm, which contains the  $n = 4, 5$  modes, for different angles of incident  $\theta$  and p-polarized light. As  $\theta$  decreases from  $90^\circ$  to  $45^\circ$ , the intensity of  $n = 5$  decreases, while the intensity of  $n = 4$  increases. Particularly, for  $\theta \leq 60^\circ$ , the mode with  $n = 4$  shows a stronger peak intensity than for  $n = 5$ , indicating a dominance of the even mode. In **Figure 5D** we plotted the phase of the z-component of the  $E$ -field,  $E_z$ , around a AgAuAg NR at 1064 nm for different values of  $\theta$ . As  $\theta$  decreases from  $90^\circ$  to  $45^\circ$ , changes in the phase maps suggest that the resonance order shifts from  $n = 5$  to  $n = 4$ .

We performed similar analyses for AgAuAg NRs with lengths from  $L = 170$  nm to 380 nm in **Figure S6** to **Figure S9**, and these simulations confirmed that only odd modes are excited for  $\theta = 90^\circ$ , whereas for  $\theta \leq 60^\circ$  even order resonances are preferred. The strong enhancement of the virtual p-polarized  $E$ -field component and the preference of even mode patterns for AgAuAg NRs, which mirrors the experimentally observed behavior in our sNSOM measurements, suggests a prominent role of the virtual field in determining the experimentally observed  $E$ -field patterns on high refractive index substrates. We also investigated the effect of lower refractive index substrates and performed additional simulations with AgAuAg NRs on  $\text{SiO}_2$  ( $n_r = 1.45$ ) (**Figure S10** to **Figure S13**). We found that the preferential excitation of even modes on lower refractive index substrates is possible but requires a shallower angle of incidence of  $\theta \leq 45^\circ$ .

In Si-supported AgAuAg NRs with  $L = 88.1 - 749.0$  nm we experimentally observed SPP Fabry-Perot resonances with  $n = 1 - 12$ . Intriguingly, the slope of the  $L(n)$  relationship for AgAuAg NRs differed

for short and long NRs. The experimental  $L(n)$  relationship for AgAuAg NRs is well described by  $L_{exp1}(n) = (+38.6 + 49.6n) \text{ nm}$  (**Figure 5E1**) for short rods ( $L < 200 \text{ nm}$ ,  $n < 4$ ) and  $L_{exp2}(n) = (+36.1 + 59.2n) \text{ nm}$  (**Figure 5E2**) for long rods ( $L > 200 \text{ nm}$ ,  $n > 4$ ). We also evaluated the  $E$ -field distribution along AgAuAg, Ag, and Au nanostructures as function of their length  $L$  in the simulation model. **Figure 5B** shows that standing plasmon waves provide much higher  $E$ -field at the interface between AgAuAg NR and Si than at the interface between AgAuAg NR and air. Given this large difference in intensity, we focused in the simulations on this interface and performed model calculations with NRs embedded in Si using an excitation wavelength of 1064 nm and an angle of incidence of  $\theta = 60^\circ$  (see Methods section). The simulated near-field maps are shown in **Figure S14 – Figure S16**. As expected, for all three rods  $L$  increases as function of  $n$ . The simulated  $L$  vs.  $n$  relationships are given as  $L_{AgAuAg1}(n) = (+20.0 + 46.0n) \text{ nm}$  (**Figure 5E1**) for short NRs with  $L < 200 \text{ nm}$  ( $n < 4$ ) and  $L_{AgAuAg2}(n) = (-29.8 + 59.3n) \text{ nm}$  (**Figure 5E2**) for  $L > 200 \text{ nm}$  ( $n > 4$ ). The slope of the experimental and simulated  $L(n)$  relationships for AgAuAg NRs are essentially identical. The  $L(n)$  relationships for pure Ag NRs and pure Au NRs,  $L_{Ag}(n) = (-7.8 + 57.2n) \text{ nm}$ , and  $L_{Au}(n) = (-3.3 + 46.0n) \text{ nm}$ , are included in both **Figure 5E1** and **Figure 5E2** for completeness. For  $L < 200 \text{ nm}$  ( $n < 4$ ) both the simulated and experimental slopes of  $L(n)$  for AgAuAg NRs are similar to those of Au NRs while for longer AgAuAg NRs ( $L > 200 \text{ nm}$ ,  $n > 4$ ) the slopes of  $L(n)$  are close to those of Ag NRs and distinctly different from Au NRs. These findings imply i.) that the SPP wavelength in AgAuAg NR changes with  $L$  as the AgAuAg NRs become more and more Ag in nature, and ii.) that the Au BP core in the AgAuAg heterostructure does not significantly affect the guided plasmon in sufficiently long NRs. The latter finding is in general agreement with previous FDTD simulations by Zhuo *et al.*<sup>13</sup>.

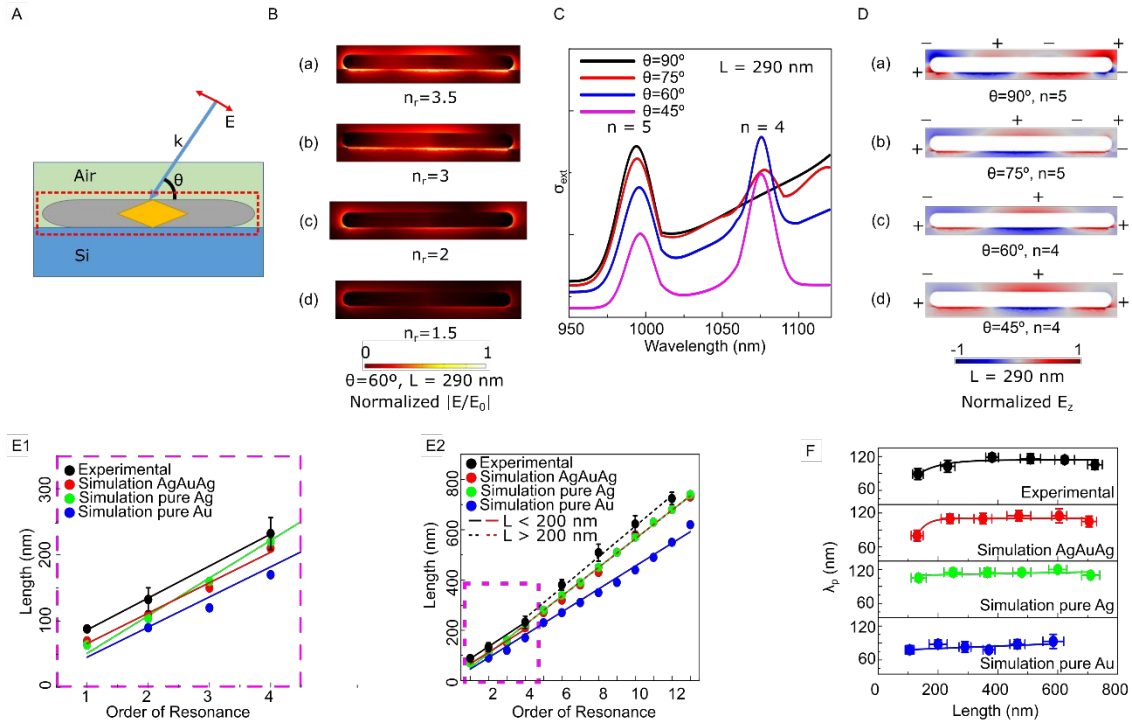


Figure 5. (A) Simulation setup of substrate-supported AgAuAg NRs. (Ba) – (Bd) Normalized  $|E/E_0|$  of AgAuAg NRs ( $L = 290$  nm) on substrates with (bottom to top) increasing refractive index,  $n_r$ . (C) Calculated extinction cross sections of AgAuAg NRs ( $L = 290$  nm) with different angles of incidence. (Da) – (Dd) Simulated normalized  $E_z$  around AgAuAg NRs ( $L = 290$  nm) with different angles of incidence. The images show in the YZ plane. (E1) and (E2) Experimental and simulated  $L$  vs.  $n$  relationship for AgAuAg NRs, Ag NRs, and Au NRs as a function of resonance order  $n$ , for (E1) short nanorods ( $L < 200$  nm,  $n < 4$ ). (F) Experimentally measured propagation wavelength ( $\lambda_p$ ) for AgAuAg NRs and calculated  $\lambda_p$  for Ag NR, Au NR, and AgAuAg as a function of  $L$ .

For NRs with sufficient length that the restructuring of the ends is completed ( $n \geq 2$ ;  $L > 130$  nm), it is justified to assume that the phase shifts,  $\delta\varphi$ , for rods of order  $n$  and  $n+2$  are identical. In that case, it follows from the Fabry-Perot resonance condition that the effective wavelength of the standing plasmon mode is  $\lambda_p = \Delta L = 2\pi/\gamma$ , where  $\Delta L$  corresponds to the difference in length between resonant orders  $n$  and  $n+2$ . We plotted the experimental  $\lambda_p$  for AgAuAg NRs and the simulated  $\lambda_p$  for AgAuAg NRs, Ag NRs and Au NRs in **Figure 5F**. The simulated propagation wavelength of Ag/Si interface ( $\lambda_p = 113.5 \pm 4.7$  nm) is larger than Au/Si interface ( $\lambda_p = 90.8 \pm 6.7$  nm). The experimental propagation wavelength in AgAuAg bimetallic nanostructure evolves from  $\lambda_p = 89.0 \pm 9.8$  nm to  $113.8 \pm 12.5$  nm as the length increases from  $132.6 \pm 17.6$  nm to  $724.5 \pm 24.5$  and the NR becomes more Ag in nature. This trend is in good agreement

with the simulated data for AgAuAg NRs, which change from  $\lambda_p = 80.0 \pm 9.4$  nm to  $111.0 \pm 13.0$  nm in the same  $L$ -range as the length increases from  $130.0 \pm 20.0$  nm to  $705.0 \pm 25.0$  nm. Previous experimental studies of Au NRs with sNSOM reported a propagation wavelength at the interface of silica and Au of  $\lambda_p = 372.8$  nm,<sup>29</sup> and EELs measurements of Ag NRs found an effective propagation wavelength (in vacuum) of  $\lambda_p = \sim 450$  nm.<sup>50</sup> The shorter propagation wavelengths in our experiments is consistent with the higher refractive index of the Si substrate. To support our assumption and to validate the accuracy of our simulation model, we calculated our AgAuAg NRs structures on silica substrate and in vacuum as shown in **Figure S17** and **Figure S18**, which led to longer propagation wavelengths of  $\lambda_p = 334.4 \pm 19.1$  nm and  $\lambda_p = 447.5 \pm 23.5$  nm, respectively.

## Conclusion

In this study, we revisited the evolution of the far-field spectrum during heteroepitaxial growth of Ag on Au BPs, which gradually transforms the Au BP into a AgAuAg bimetallic NR. In good agreement with previous studies,<sup>12</sup> we detected an initial blue-shift during a restructuring of the BP tip that is followed by a red-shift once the BP tips are blunted, and the structure is converted into a NR that increases its AR upon further addition of Ag. We quantified the contributions from changes in the morphology and dielectric function to the initial blue-shift through electromagnetic simulations and found that changes in the dielectric function and the tip morphology both contribute to the spectral blue-shift observed during transformation of the Au BP into a AgAuAg NR through deposition of Ag. While the contribution from the morphological change to the spectral blue-shift of the longitudinal dipolar mode increases with tip diameter, the shift of the vertical dipolar mode is dominated by the change in the dielectric function.

After validating the successful synthesis of AgAuAg NRs through structural analysis and characterization of their far-field properties, we then mapped the near-field around the characterized AgAuAg NRs with lengths between  $L = 88.1$  nm and  $749.0$  nm on a Si support using scattering-type near-

field scanning optical microscopy (sNSOM) at a constant wavelength of 1064 nm. These experiments revealed Fabry-Perot like resonances formed by guided plasmons, whose mode order increased with length of the NRs. For NRs with length between  $L = 88.1$  nm and 749.0 nm, we detected orders between  $n = 1 - 12$ . Intriguingly, the near-field scans revealed a predominance of even modes in AgAuAg NRs on a Si substrate for higher orders  $n > 1$ . The p-polarized component of the virtual  $E$ -field around the NR is one important factor that determines the detected near-field. Our simulations show that the p-component of the virtual  $E$ -field is enhanced on the high refractive index substrate and that it shows a phase pattern along the NR that is consistent with an even mode symmetry as observed experimentally. The (image) charge accumulation at the interface between metal NR and the high refractive index substrate enhances the p-component and contributes to the predominance of the even modes observed in the experiment. The effective wavelength of the propagating surface plasmon on the Si-supported AgAuAg NRs was determined for NRs of different lengths and we found that it changes from  $89.0 \pm 9.8$  nm to  $113.8 \pm 12.5$  nm as the length develops from  $132.6 \pm 17.6$  nm to  $724.5 \pm 24.5$  nm. For sufficient long NR ( $L > 200$  nm), the optical properties of bimetallic nanostructure are almost the same as “pure” Ag NRs.

### **Acknowledgement**

This work was supported in part by the National Science Foundation through grants DMR-1429437 and CHE-1808241.

## Methods

*Materials and chemicals.* Tetrachloroauric acid ( $\text{HAuCl}_4$ ,  $\geq 99\%$ ), hexadecyltrimethylammonium chloride (CTAC, 25 wt % in water), hexadecyltrimethylammonium bromide (CTAB,  $\geq 99\%$ ), citric acid ( $\geq 99.5\%$ ), sodium borohydride ( $\text{NaBH}_4$ ), silver nitrate ( $\text{AgNO}_3$ ,  $\geq 99\%$ ), hydrochloric acid (HCl, 37%), L-ascorbic acid (AA,  $\geq 99\%$ ) were purchased from Sigma-Aldrich.  $\text{HS}-(\text{CH}_2)_2-\text{O}(\text{CH}_2\text{CH}_2\text{O})_n-\text{COOH}$  (MW = 1000 g/mol) was purchased from Creative PEGWorks. All chemicals were used without further purification.

*Synthesis of nanoparticles.* The Au BPs were synthesized following a published procedure by medium seed growth reaction.<sup>20</sup>  $\text{HAuCl}_4$  (10 mL, 0.25 mM) in an aqueous CTAC solution (50 mM) was reduced to form initial gold seeds by addition of freshly prepared  $\text{NaBH}_4$  (0.25 mL, 25 mM) in the presence of citric acid (5 mM) under vigorous stirring at room temperature. Then, after 2 minutes, the seed solution was transferred and heated in an oil bath at 80 °C for 90 minutes under gentle stirring. Finally, the thermally treated seed solution was removed from the bath and stored at room temperature. The Au BPs were grown by injecting 1.1 mL gold seeds under vigorous stirring to an aqueous growth solution containing CTAB (100 mL, 100 mM),  $\text{HAuCl}_4$  (5 mL, 10 mM),  $\text{AgNO}_3$  (1 mL, 10 mM), HCl (2 mL, 1M) and L-ascorbic acid (0.8 mL, 100 mM). The mixture was kept at 30 °C overnight. The nanoparticles were cleaned again through repeated centrifugation and resuspension and then purified following described procedures to increase the Au BPs product yield,<sup>1,12-14</sup> and finally resuspended in 40 mL DI water. For the growth of AgAuAg bimetallic nanostructure, 2 mL Au BP solution and 0.7 mL CTAC 25 wt.% solution were added to 5 mL DI water and different amounts of a 0.1 mM  $\text{AgNO}_3$  solution. The mixture was stirred vigorously at 75 °C. And finally, 1 mL 0.2 mM L-ascorbic acid was quickly injected as excessive reduction agent. After 4 hours, the nanoparticles were centrifuged and redispersed in DI water repeatedly to remove CTAC ligands. PEGylating process is necessary to obtain stable bimetallic nanoparticles. 5  $\mu\text{L}$  of 10 mM  $\text{HS}-(\text{CH}_2)_2-\text{O}(\text{CH}_2\text{CH}_2\text{O})_n-\text{COOH}$  (MW = 1000 g/mol) was added to 1 mL of AgAuAg NRs in the presence of 3% v/v

of Tween 20. The samples were incubated 2 hours and washed by centrifugation and subsequent resuspension in DI as the final product.

*TEM imaging and elemental mapping.* TEM images were taken with a FEI Tecnai Osiris 200 KV, and were used to determine the average size of nanoparticles. STEM and elemental mapping images were acquired and analyzed to determine the elemental composition of the nanoparticles.

*UV-Vis-NIR spectrum measurement.* The spectrum of diluted samples in heavy water were recorded by UV-Vis-NIR spectrometer (Cary 5000) from 400 nm to 1800 nm at the resolution of 2 nm. The recorded spectrum were normalized and fitted by the Gaussian peak to determine the resonance peak position and FWHM.

*Scattering-type near-field scanning optical microscope (sNSOM) measurements.* The near-field scan was performed by near-field scanning optical microscope (Neaspec, Nano Imaging Module) with fixed wavelength laser of 1064 nm. AFM tapping mode scanning was performed with a commercial AFM silicon tip (Nano World), which oscillates around a mean distance of about 10 nm – 20 nm above the surface. The sample was prepared by evaporating 5  $\mu$ l of a 200  $\times$  fold diluted sample solution on a 1 cm  $\times$  1 cm  $\times$  1 mm silicon wafer. The fourth harmonic of the near-field amplitude (O4A) and the third harmonic of near-field phase (O3P) were used for analysis. The measured data was processed with Gwyddion for background correction and signal smoothing, and plotted with Matlab.

*Electromagnetic simulations.* All structures were designed using the electromagnetic design module in COMSOL Multiphysics. As shown in the inset mesh plot of **Figure 2(B)** and **Figure 4(A)** AgAuAg NRs were modeled and meshed. Based on the TEM evaluation of the synthesized nanostructures, Au BPs were described by 2 adjacent cones with tip radius of 2.5 nm, width of 25 nm and length of 70 nm. For AgAuAg NRs in the blue-shifted spectral range, we approximated the grown silver shell with 2 adjacent cones with different tip radius  $r_{\text{core}} < r_{\text{Ag}} < d$ , where  $r_{\text{core}}$  and  $r_{\text{Ag}}$  are the radii of the Au BP core and AgAuAg NR, respectively,  $d$  is the width of Au BP. AgAuAg NRs in the red-shifted spectral range were modelled as

cylindrical nanorods with different lengths. We applied the refractive indexes of Au, Ag and water to the system for calculation. For single nanoparticle extinction cross section simulation, the structures were surrounded by a sphere representing the surrounding medium of water, and enclosed by a perfect matching layer, which prevented unwanted reflections from the outside boundary. For  $n = 1$  and  $n = 3$  resonance order simulation, we set the angle of incident  $\theta = 90^\circ$  while in order to effectively induce the  $n = 2$  mode, we set the angle of incident  $\theta = 45^\circ$  (as shown in the inset of **Figure 3A**). In both cases, the light was polarized along the long axis of nanorod.

For simulations of the near-field of colloidal Au BP or AgAuAg NR, the nanoparticle was dispersed in water ( $n_r = 1.33$ ). Resonances with  $n = 1, 3$  were induced with normal incident  $\theta = 90^\circ$ , and the  $n = 2$  resonance mode was excited with an angle of incidence of  $\theta = 45^\circ$  (as shown in the inset of **Figure 3A**). In both cases, the light was polarized along the long axis of the nanorod.

For simulations of the AgAuAg NR on substrate, as shown in **Figure 5A**, AgAuAg NR is placed at the interface of silicon or silica substrate and air medium, and is excited with virtual p-polarized light with angle of incident of  $\theta$ . We applied the refractive indexes of Au, Ag, silicon ( $n_{\text{Si}} = 3.5$ ) and quartz ( $n_{\text{quartz}} = 1.45$ ) to the system for calculation. We evaluated the field distribution of the  $E_z$  component of the field in the YZ plane to estimate the resonance order.

For propagation wavelength calculation, we used a variable meshing with mesh sizes down to 0.5 nm in the immediate vicinity of the nanoparticles. The simulations were performed for AgAuAg NRs, pure Ag NRs and pure Au NRs of different lengths embedded in Si at a wavelength of 1064 nm using the refractive indexes of Au, Ag and Si. We applied corrected silicon refractive index for calculation ( $n_{\text{eff}} = 0.9 \times n_{\text{Si}} + 0.1 \times n_{\text{air}}$ ), in order to correct the existing air medium. In order to excite both even and odd resonance, the AgAuAg NR is excited with the asymmetric illumination at incident angle of incident light  $\theta = 60^\circ$ . We calculated the field distribution of the  $E_z$  component (real value and argument of  $E_z$ ) of the field in the XY plane with a Z average value  $\sim 11$  nm above the nanostructure.

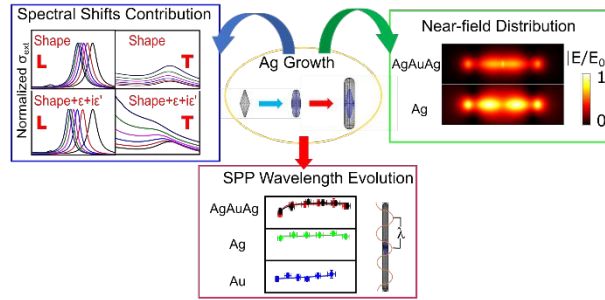
**Reference**

- 1 G. Park, D. Seo, J. Jung, S. Ryu and H. Song, *J. Phys. Chem. C*, 2011, **115**, 9417–9423.
- 2 H. Lee, S. Habas, G. Somorjai and P. Yang, *J. Am. Chem. Soc.*, 2008, **130**, 5406–5407.
- 3 Y.-C. Tsao, S. Rej, C.-Y. Chiu and M. Huang, *J. Am. Chem. Soc.*, 2014, **136**, 396–404.
- 4 L. Han, C. Li, T. Zhang, Q. Lang and A. Liu, *ACS Appl. Mater. Inter.*, 2015, **7**, 14463–14470.
- 5 G. Bhattacharjee, M. Bhattacharya, A. Roy, D. Senapati and B. Satpati, *ACS Appl. Nano Mater.*, 2018, **1**, 5589–5600.
- 6 B. Lim, H. Kobayashi, T. Yu, J. Wang, M. Kim, Z.-Y. Li, M. Rycenga and Y. Xia, *J. Am. Chem. Soc.*, 2010, **132**, 2506–2507.
- 7 X. Zhu, H. K. Yip, X. Zhuo, R. Jiang, J. Chen, X. M. Zhu, Z. Yang and J. Wang, *J. Am. Chem. Soc.*, 2017, **139**, 13837–13846.
- 8 B. Rodríguez-González, A. Burrows, M. Watanabe, C. J. Kiely and L. M. L. Marzán, *J. Mater. Chem.*, 2005, **15**, 1755–1759.
- 9 C. S. Ah, S. Do Hong and D. J. Jang, *J. Phys. Chem. B*, 2001, **105**, 7871–7873.
- 10 M. Liu and P. Guyot-Sionnest, *J. Phys. Chem. B*, 2005, **109**, 22192–22200.
- 11 M. Jones, K. Osberg, R. MacFarlane, M. Langille and C. Mirkin, *Chem. Rev.*, 2011, **111**, 3736–3827.
- 12 X. Zhu, X. Zhuo, Q. Li, Z. Yang and J. Wang, *Adv. Funct. Mater.*, 2016, **26**, 341–352.
- 13 X. Zhuo, X. Zhu, Q. Li, Z. Yang and J. Wang, *ACS Nano*, 2015, **9**, 7523–7535.
- 14 M. Mayer, L. Scarabelli, K. March, T. Altantzis, M. Tebbe, M. Kociak, S. Bals, F. J. García De Abajo, A. Fery and L. M. Liz-Marzán, *Nano Lett.*, 2015, **15**, 5427–5437.

- 15 L. Dai, L. Song, Y. Huang, L. Zhang, X. Lu, J. Zhang and T. Chen, *Langmuir*, 2017, **33**, 5378–5384.
- 16 Y. Okuno, K. Nishioka, A. Kiya, N. Nakashima, A. Ishibashi and Y. Niidome, *Nanoscale*, 2010, **2**, 1489–1493.
- 17 Y. Wu, P. Jiang, M. Jiang, T.-W. Wang, C.-F. Guo, S.-S. Xie and Z.-L. Wang, *Nanotechnology*, 2009, **20**, 305602.
- 18 C. Li, L. Sun, Y. Sun and T. Teranishi, *Chem. Mater.*, 2013, **25**, 2580–2590.
- 19 J. Zeng, S. Roberts and Y. Xia, *Chem. - A Eur. J.*, 2010, **16**, 12559–12563.
- 20 A. Sánchez-Iglesias, N. Winckelmans, T. Altantzis, S. Bals, M. Grzelczak and L. Liz-Marzán, *J. Am. Chem. Soc.*, 2017, **139**, 107–110.
- 21 Y. Song, M. A. Hickner, S. R. Challa, R. M. Dorin, R. M. Garcia, H. Wang, Y. Jiang, P. Li, Y. Qiu, F. Van Swol, C. J. Medforth, J. E. Miller, T. Nwoga, K. Kawahara, W. Li and J. A. Shelnutt, *Nano Lett.*, 2009, **9**, 1534–1539.
- 22 R. Gordon, *Opt. Express*, 2009, **17**, 18621–18629.
- 23 B. Khlebtsov and N. Khlebtsov, *J. Phys. Chem. C*, 2007, **111**, 11516–11527.
- 24 T. Taminiau, F. Stefani and N. Hulst, *Nano Lett.*, 2011, **11**, 1020–1024.
- 25 M. Liu, T. Lee, S. K. Gray, P. Guyot-Sionnest and M. Pelton, *Phys. Rev. Lett.*, 2009, **102**, 107401.
- 26 E. Cubukcu and F. Capasso, *Appl. Phys. Lett.*, 2009, **95**, 201101.
- 27 Q. Li, X. Zhuo, S. Li, Q. Ruan, Q. H. Xu and J. Wang, *Adv. Opt. Mater.*, 2015, **3**, 801–812.
- 28 C. Fang, G. Zhao, Y. Xiao, J. Zhao, Z. Zhang and B. Geng, *Sci. Rep.*, 2016, **6**, 36706.
- 29 J. Dorfmueller, R. Vogelgesang, R. T. Weitz, C. Rockstuhl, C. Etrich, T. Pertsch, F. Lederer and K.

- Kern, *Nano Lett.*, 2009, **9**, 2372–2377.
- 30 J. Martin, M. Kociak, Z. Mahfoud, J. Proust, D. Gérard and J. Plain, *Nano Lett.*, 2014, **14**, 5517–5523.
- 31 G. Cheng, D. Wang, S. Dai, X. Fan, F. Wu, X. Li and C. Zeng, *Nanoscale*, 2018, **10**, 16314–16320.
- 32 A. Arcangeli, F. Rossella, A. Tomadin, J. Xu, D. Ercolani, L. Sorba, F. Beltram, A. Tredicucci, M. Polini and S. Roddaro, *Nano Lett.*, 2016, **16**, 5688–5693.
- 33 S. Mastel, M. Lundeberg, P. Alonso-Gonzalez, Y. Gao, K. Watanabe, T. Taniguchi, J. Hone, F. Koppens, A. Nikitin and R. Hillenbrand, *Nano Lett.*, 2017, **17**, 6526–6533.
- 34 X. Chen, D. Hu, R. Mescall, G. You, D. Basov, Q. Dai and M. Liu, *Adv. Mater.*, 2019, **31**, 1804774.
- 35 R. Deshpande, V. Zenin, F. Ding, N. Mortensen and S. Bozhevolnyi, *Nano Lett.*, 2018, **18**, 6265–6270.
- 36 P. Pons-Valencia, F. Alfaro-Mozaz, M. Wiecha, V. Bielek, I. Dolado, S. Velez, P. Li, P. Alonso-González, F. Casanova, L. Hueso, L. Martin-Moreno, R. Hillenbrand and A. Nikitin, *Nat. Commun.*, 2019, **10**, 3242.
- 37 F. J. Alfaro-Mozaz, S. V. Dolado, I. Dolado, M. Autore, S. Mastel, F. Casanova, L. E. Hueso, P. Li, A. Y. Nikitin and R. Hillenbrand, *Nat. Commun.*, 2017, **8**, 15624.
- 38 T. Neuman, P. Alonso-González, A. Garcia-Etxarri, M. Schnell, R. Hillenbrand and J. Aizpurua, *Laser Photonics Rev.*, 2015, **9**, 637–649.
- 39 F. Keilmann, A. J. Huber and R. Hillenbrand, *J. Infrared Milli Terahz Waves*, 2009, **30**, 1255–1268.

- 40 J. Zhang, X. Chen, S. Mills, T. Ciavatti, Z. Yao, R. Mescall, H. Hu, V. Semenenko, Z. Fei, H. Li, V. Perebeinos, H. Tao, Q. Dai, X. Du and M. Liu, *ACS Photonics*, **5**, 2645–2651
- 41 N. Qin, S. Zhang, J. Jiang, S. G. Corder, Z. Qian, Z. Zhou, W. Lee, K. Liu, X. Wang, X. Li, Z. Shi, Y. Mao, H. A. Bechtel, M. C. Martin, X. Xia, B. Marelli, D. L. Kaplan, F. G. Omenetto, M. Liu and T. H. Tao, *Nat. Commun.*, 2016, **7**, 13079.
- 42 M. Wagner and M. Liu, *Nat. Photonics*, 2016, **10**, 210–211.
- 43 E. Encina and E. Coronado, *J. Phys. Chem. C*, 2007, **111**, 16796–16801.
- 44 E. Encina and E. Coronado, *J. Phys. Chem. C*, 2008, **112**, 9586–9594.
- 45 H. Chen, L. Shao, Q. Li and J. Wang, *Chem. Soc. Rev.*, 2013, **42**, 2679–2724.
- 46 A. B. Khanikaev, N. Arju, Z. Fan, D. Purtseladze, F. Lu, J. Lee, P. Sarriguarte, M. Schnell, R. Hillenbrand, M. A. Belkin and G. Shvets, *Nat. Commun.*, 2016, **7**, 12045.
- 47 X. Zhuo, H.-K. Yip, Q. Ruan, T. Zhang, X. Zhu, J. Wang, H. Lin, J. Xu and Z. Yang, *ACS Nano*, 2018, **12**, 1720–1731.
- 48 M. Schnell, P. Sarriguarte, T. Neuman, A. B. Khanikaev, G. Shvets, J. Aizpurua and R. Hillenbrand, *Nano Lett.*, 2016, **16**, 663–670.
- 49 H. Chen, M. Tian, Z. Shouren, Z. Jin, B. Yang and J. Wang, *ACS Nano*, 2011, **5**, 4865–4877.
- 50 D. Rossouw, M. Couillard, J. Vickery, E. Kumacheva and G. A. Botton, *Nano Lett.*, 2011, **11**, 1499–1504.



The effect of composition and tip morphology on the far-field optical response of gold nanobipyramids upon heteroepitaxial deposition of silver is quantified and the near-field associated with standing plasmon waves of silver-gold-silver nanorods on silicon substrates is measured.